Supplementary

Oriented Bi_2Te_3-based films enabled high performance planar thermoelectric cooling device for hot spot elimination

Guoying Dong[1,#], Jianghe Feng[1#],Guojuan Qiu[1, #], Yuxuan Yang[2], Haijun Wu[2,*], Qiyong Chen[3], Yang Xiong[1], Yifeng Ling[1], Lili Xi[3], Chen Long[1], Jibao Lu[1], Yixin Qiao[1], Guijuan Li[1], Juan Li[1*], Ruiheng Liu[1,*], Rong Sun[1]

[1]Shenzhen Institute of Advanced Electronic Materials, Shenzhen Institute of Advanced Technology, Chinese Academy of Sciences, Shenzhen 518055, China
[2] State Key Laboratory for Mechanical Behavior of Materials, Xi'an Jiaotong University, Xi'an 710049, China
[3]Materials Genome Institute, Shanghai University, Shanghai 200444, China

[#] These authors contribute equally to this work.
[*]Corresponding authors: wuhaijunnavy@xjtu.edu.cn; j.li1@siat.ac.cn; rh.liu@siat.ac.cn

Materials and methods:

Phase and Microstructure Characterization: The room temperature X-ray diffraction (XRD) was carried out for obtained n-type Bi_2Te_{3+x} and p-type $Bi_{0.4}Sb_{1.6}Te_{3+x}$ films after the annealing process with Bruker D8 Advance SS/ 18 kW, which is equipped with Cu Kα radiation (λ_1 = 1.54056 Å, λ_2 = 1.54443 Å) and a PIXcel detector, the current maintained at 40 mA and the working voltage was set as 40 kV. The field-emission scanning electron microscope (SEM, Thermo Scientific Apreo 2 S HiVac, 5 kV) equipped with an energy dispersive spectroscopy (EDS) is adopted to characterize the microstructure and composition. The orientation factor F of the films were calculated using the formula $F = (P_i - P_0)/(1 - P_0)$, where $P_i = I(00l)/\sum I(hkl)$, $P_0 = I_0(00l)/\sum I_0(hkl)$, $I(00l)$ is the $(00l)$ plane diffraction intensity, P_i is the intensity ratio of the $(00l)$ plane and $I(hkl)$ is the diffraction peaks intensity. $I(00l)$, P_0 and $I_0(hkl)$ were the parameters of the standard peaks (PDF no. 15-0863).

TE Property Measurement: The in-plane resistivity, Seebeck coefficient, carrier concentration and Hall mobility were simultaneously measured by a home-built apparatus from 300 to 420 K. The Seebeck coefficient was obtained from the slope of the thermopower vs. temperature difference from 0 to 5 K[1]. The thermopower was measured by two Nb wires welded to the thermocouple tips, the hot and cold side temperatures were measured by two K-type thermocouples attached to the opposite edges of the film. Four probes were connected to the films for resistivity and Hall coefficient measurement by the Van der Pauw technique under a reversible magnetic field of 1.5 T. The thermal conductivity is evaluated by transient photo-electro-thermal (TPET) technique[2] for both PI substrate and deposited PI films.

DFT calculations: Density Functional Theory (DFT) calculations were performed using the Vienna *ab initio* Simulation Package (VASP)[3-5]. The generalized gradient approximation (GGA) with the Perdew, Burke, and Ernzerhof (PBE) exchange-correlation functional was employed [6] Structural optimizations were conducted until the forces on the atoms were less than 0.01 eV/Å, with the electronic energy convergence criterion set to 10^{-6} eV in the self-consistent calculations. A cutoff energy of 350 eV was used for all computations. The structural data for Bi_2Te_3 and Sb_2Te_3 were sourced from the MatHub-3d

database[7]. Defect calculations were performed using a 4×4×1 supercell containing 240 atoms, with a Γ-centered 2×2×1 k-point mesh. The effective band structures (EBS) for the defective structures were calculated using the BandUP code [8, 9].

In this study, we calculated the binding energies of various surfaces, including the (100), (110), (015), and (001) facets. By varying the interlayer distance between the exfoliated layer and the bulk material and computing the system's energy at each state, we obtained a curve depicting the variation of the system's energy as a function of the interlayer distance. The energy of the system exhibited a trend of initial decrease followed by an increase, and ultimately reached convergence as the distance was extended. The binding energy is defined as the difference between the minimum point of the system's energy and its converged value：

$$E_b = \left(E_{vally} - E_{conv}\right) / A \qquad (1)$$

where A is the surface area. E_{vally} and E_{conv} are the minimum and convergence energies of systems, respectively.

For perfect structures, both lattice constants and atomic positions for the supercells were relaxed, whereas for defective supercells, only the atomic positions were optimized. The formation energy of a point defect can be expressed as follows[10,11]:

$$E_f = E_{defect} - E_{pefect} - \sum_i n_i \mu_i \qquad (2)$$

where E_{defect} is the total energy of the defective structure, and E_{pefect} is the total energy of the perfect supercell. In the defect structure, n_i represents the number of atoms of the i-th type (either host or impurity atoms) added to ($n_i > 0$) or removed from ($n_i < 0$) the supercell during defect formation. μ_i denotes the chemical potential for the i-th type of the atom.

Supplementary

Figures

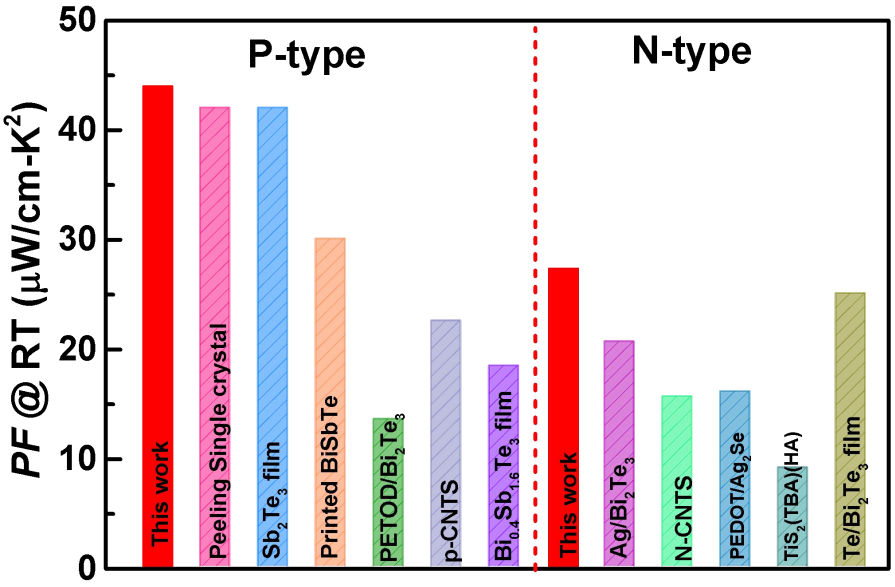

Fig. S1. **Power factor of film thermoelectric materials.** The room temperature power factor of films $Bi_{0.4}Sb_{1.6}Te_{3+x}$ (p) and Bi_2Te_{3+x} (x=0.17)(n) obtained in this work, with a comparison to that of other p-type[12-16] and n-type[17-21] thin films.

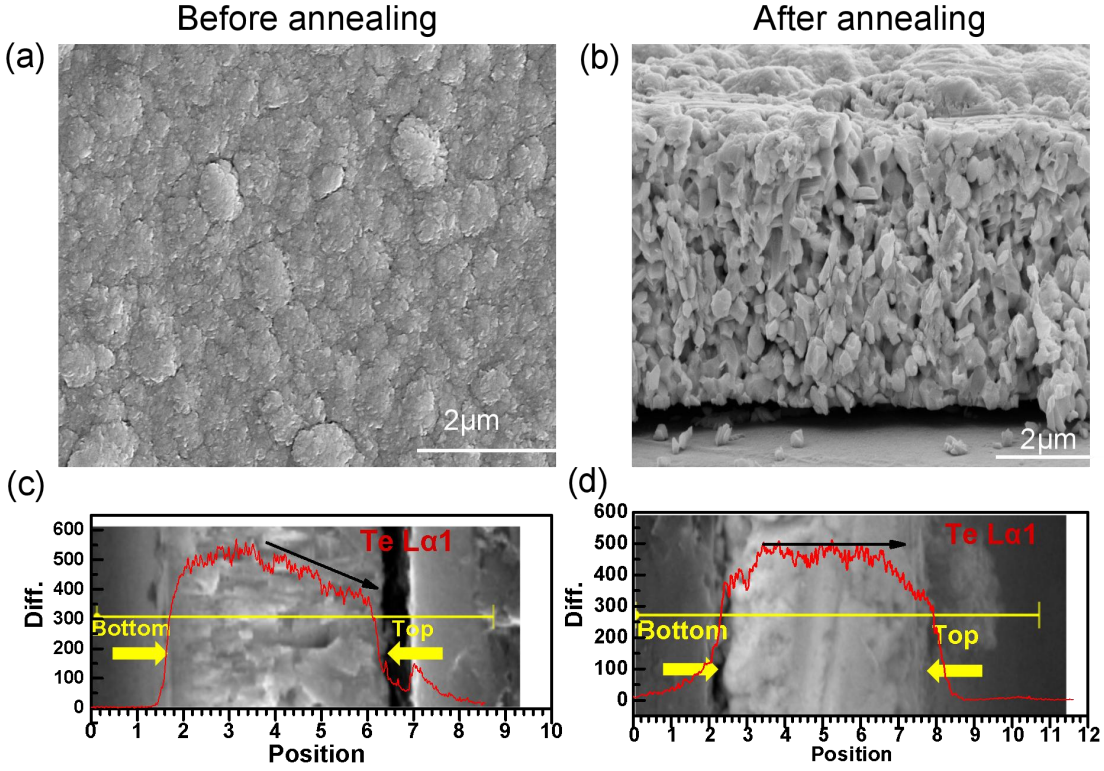

Fig. S2. **Te content distribution in the film from bottom to top**. The room temperature surface (a) and sectional (b) SEM images of n-type sample Bi_2Te_{3+x} (x=0.12), together with the Te element distribution on the sectional face from bottom to top before (c) and after (d) annealing process.

Supplementary

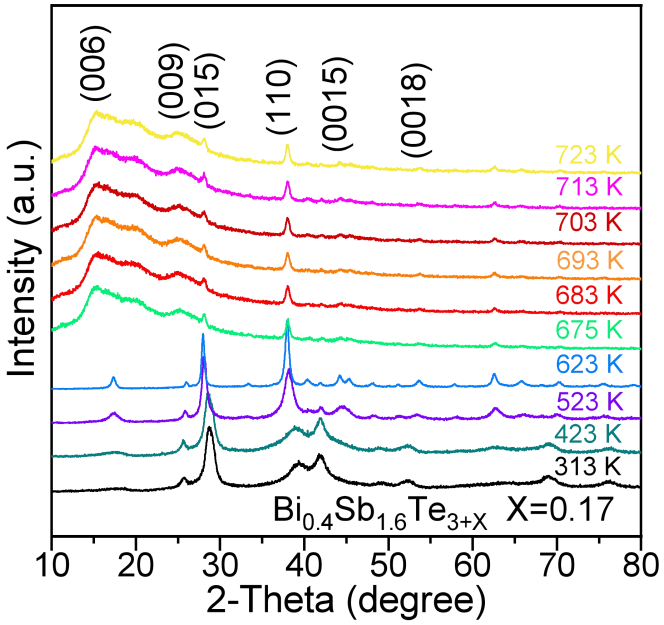

Fig. S3. **XRD patterns showing amorphous phase above 675 K.** Temperature-dependent X-ray diffraction data for sample $Bi_{0.4}Sb_{1.6}Te_{3+x}$ (x=0.17) with temperature ranging from 313 K to 723 K. The halo peak in the 2θ range 10~30° when temperature above 675 K indicating the appearance of amorphous phase Te.

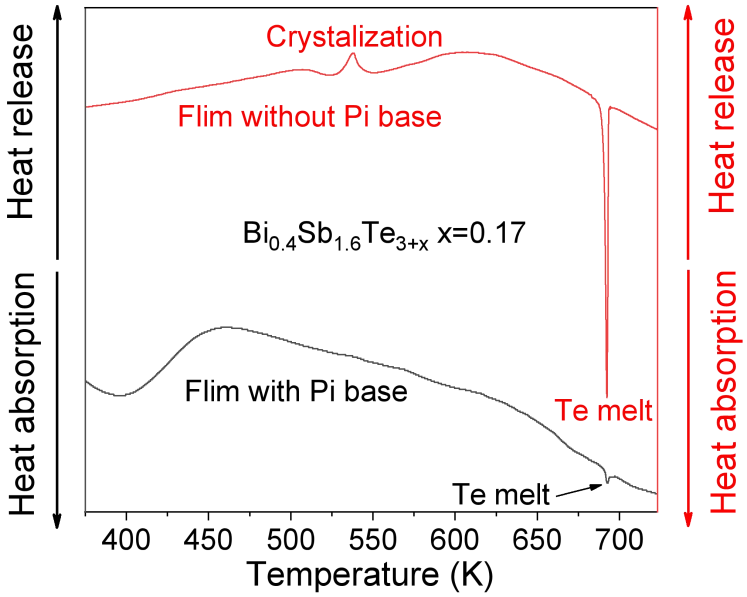

Fig. S4. **Heat flow change due to Te melting.** The temperature dependent normalized heat flow of sample $Bi_{0.4}Sb_{1.6}Te_{3+x}$ (x=0.17) with (solid black line) and without (solid red line) substate PI, the heat absorption peak at ~690 K indicates the appearance of extra Te phase transition in the film.

Supplementary

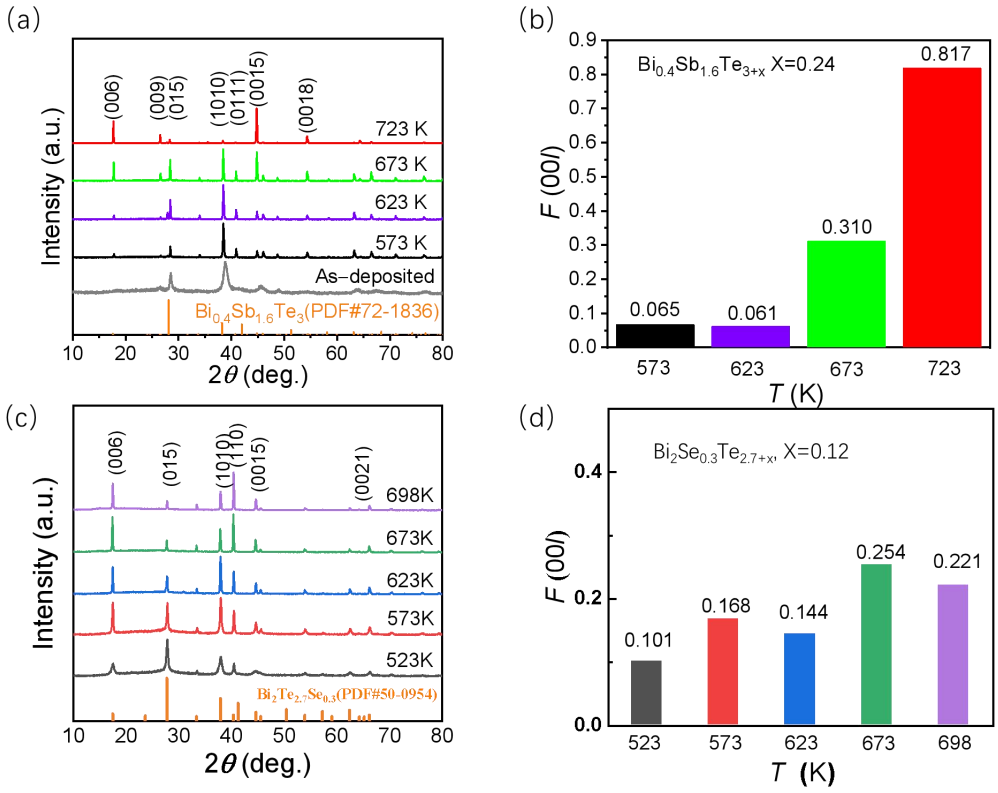

Fig. S5. **The orientation enhancement by annealing temperature for Bi_2Te_3-based samples.** (a, c) The XRD patterns and (b, d) (00*l*) orientation factor of $Bi_{0.4}Sb_{1.6}Te_{3+x}$ (x=0.24), and $Bi_2Se_{0.3}Te_{2.7+x}$ (x=0.12) samples annealed at different temperature, respectively.

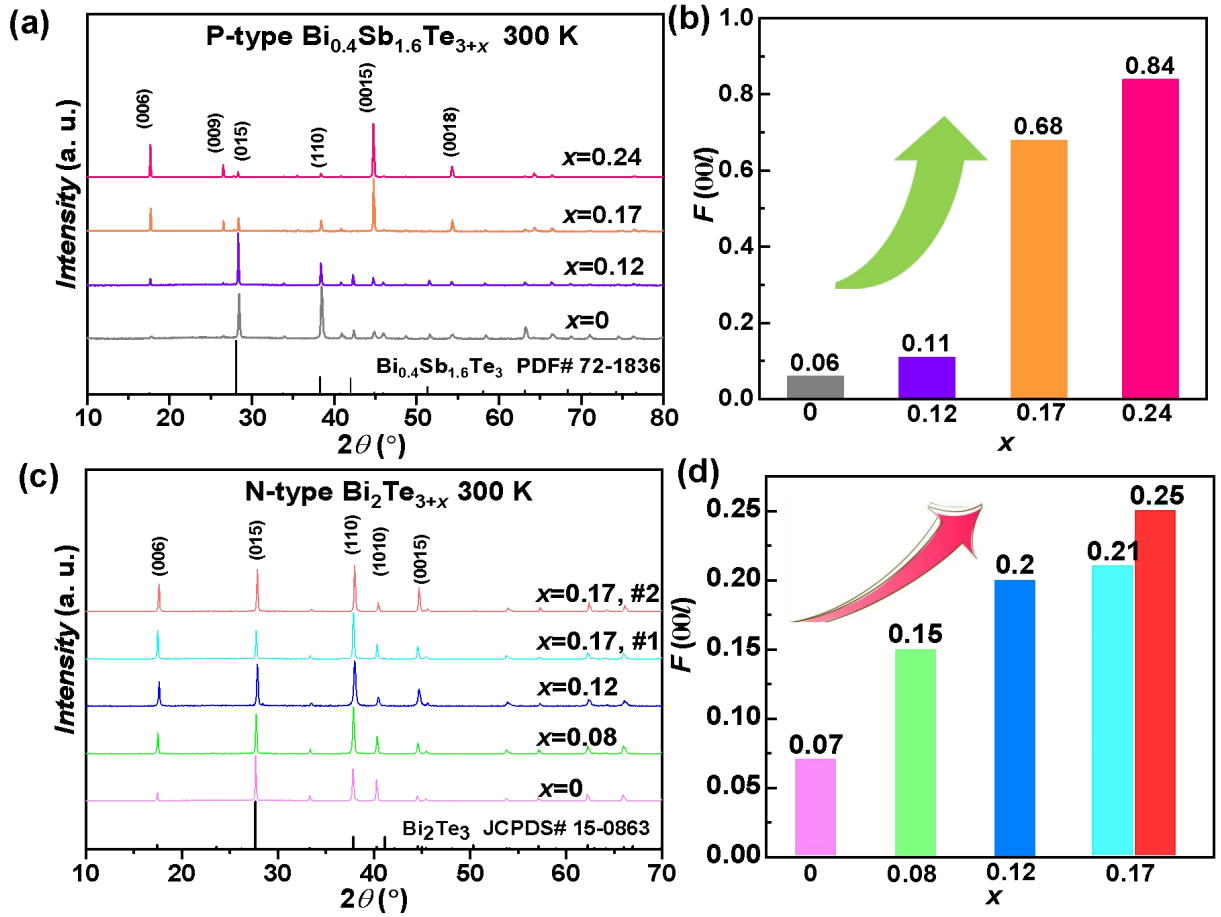

Supplementary

Fig. S6. **The orientation enhancement for Bi_2Te_3-based samples.** The room temperature XRD patterns and corresponding orientation factor for p-type $Bi_{0.4}Sb_{1.6}Te_{3+x}$ films (a, b) and n-type Bi_2Te_{3+x} films (c, d) ($0 \le x \le 0.17$); #1 and #2 represent two parallel samples.

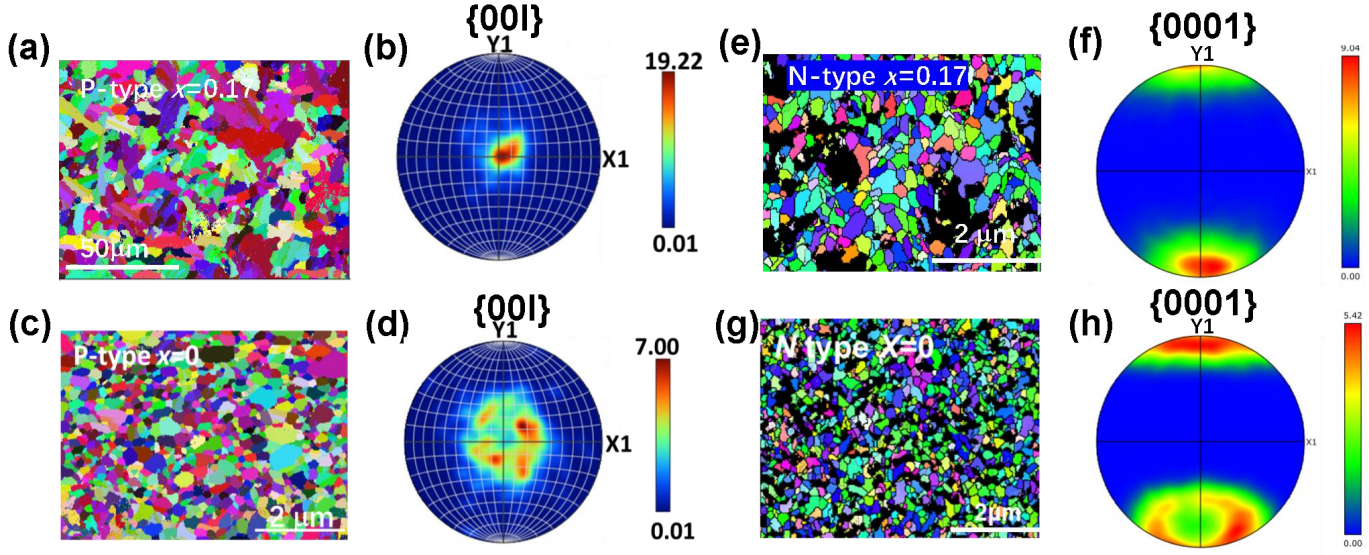

Fig. S7. **EBSD analysis for p-type and n-type samples.** The room temperature EBSD image (a) and inverse pole figure (b) for p-type $Bi_{0.4}Sb_{1.6}Te_{3+x}$ (x=0.17); EBSD image (c) and inverse pole figure (d) for p-type $Bi_{0.4}Sb_{1.6}Te_3$; EBSD image (e) and inverse pole figure (f) n-type Bi_2Te_{3+x} (x=0.17); EBSD image (g) and inverse pole figure (h) Bi_2Te_3 (c~d) films.

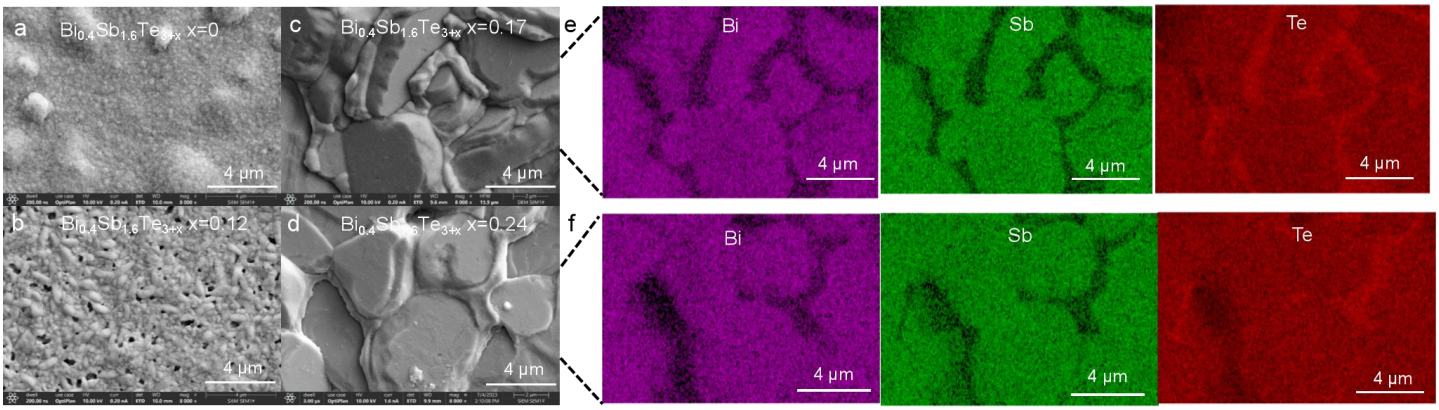

Fig. S8. **The grain size increase for p-type samples.** The room temperature SEM images of p-type $Bi_{0.4}Sb_{1.6}Te_{3+x}$(x=0, 0.12, 0.17, 0.24) samples (a~d), and the EDS analysis for x=0.17 (e~f) and x=0.24 (h~j), indicating the increase of grain size and Te-rich distribution around grain boundary.

Supplementary

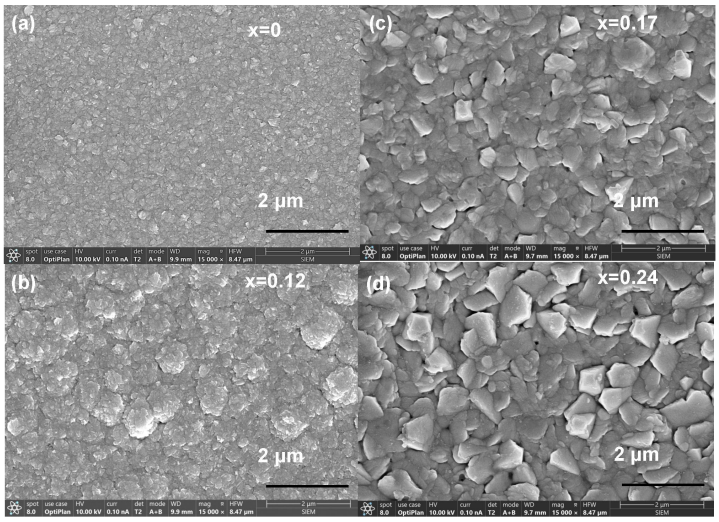

Fig. S9. **The room temperature SEM images of n-type Bi_2Te_{3+x} (x=0, 0.12, 0.17, and 0.24) (a~d) samples**

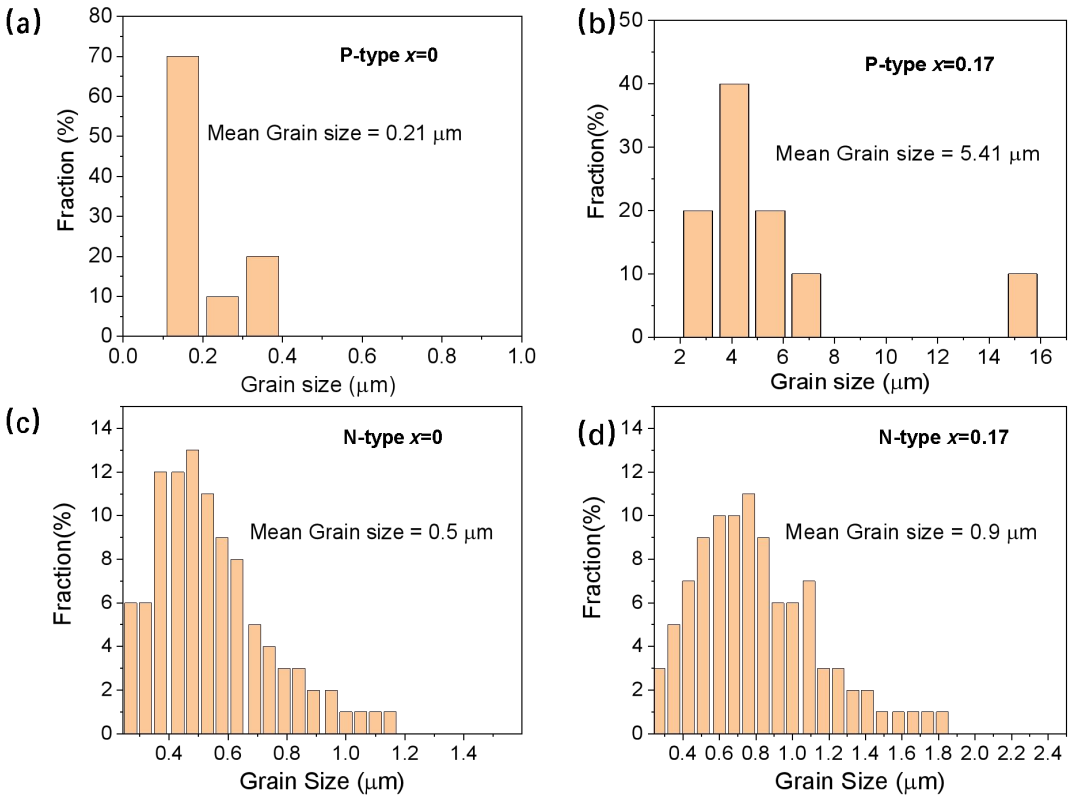

Fig. S10. **The grain size distribution for p-type $Bi_{0.4}Sb_{1.6}Te_{3+x}$ (a~b) and n-type Bi_2Te_{3+x} samples. (x=0 and 0.17) (c~d) samples**

Supplementary

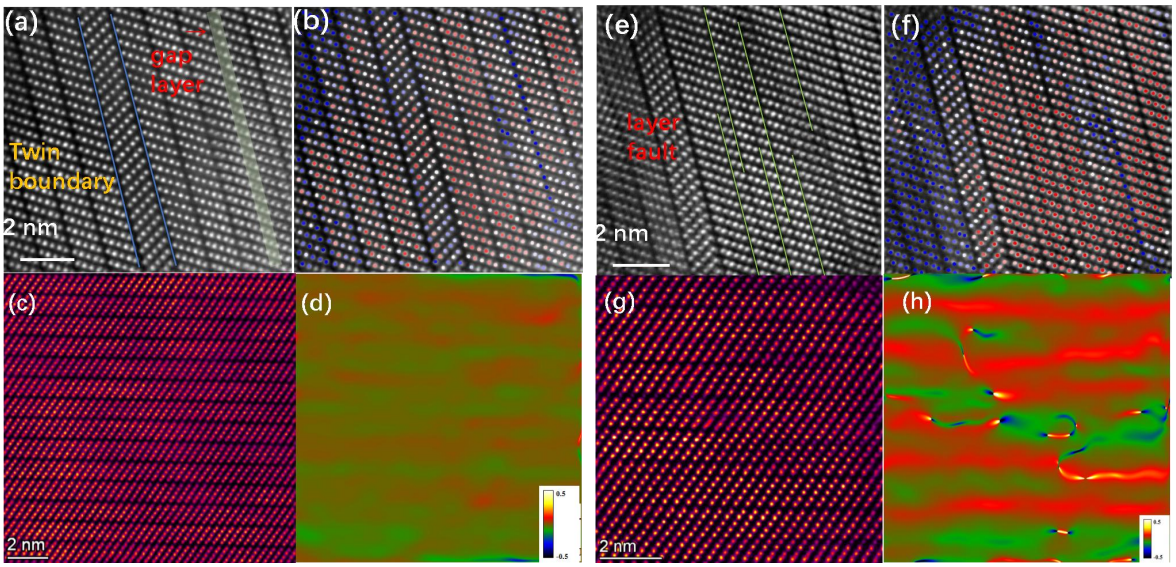

Fig.S11. **HAADF magnified images of regular and staggered layers.** HAADF magnified images (a, b) and corresponding intensity image (e, f) of atom columns utilizing the Z-contrast feature. The blue, green lines point to twin boundary and layer faults, respectively. and GPA analysis image of p-type $Bi_{0.4}Sb_{1.6}Te_{3+x}$ (x=0.17) sample; (c) are for the regular layered structure, (d) is GPA analysis image corresponding (c); (e, f, g) are for staggered stacking fault structure, and (h) is GPA analysis image corresponding (g).

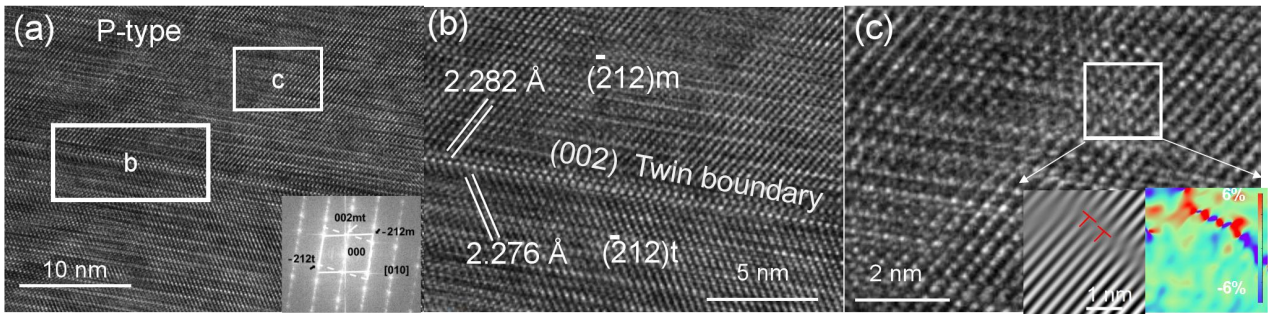

Fig.S12. **TEM image of the staggered layers and dislocation for the p-type $Bi_{0.4}Sb_{1.6}Te_{3+x}$ (x=0.17) sample.**

Supplementary

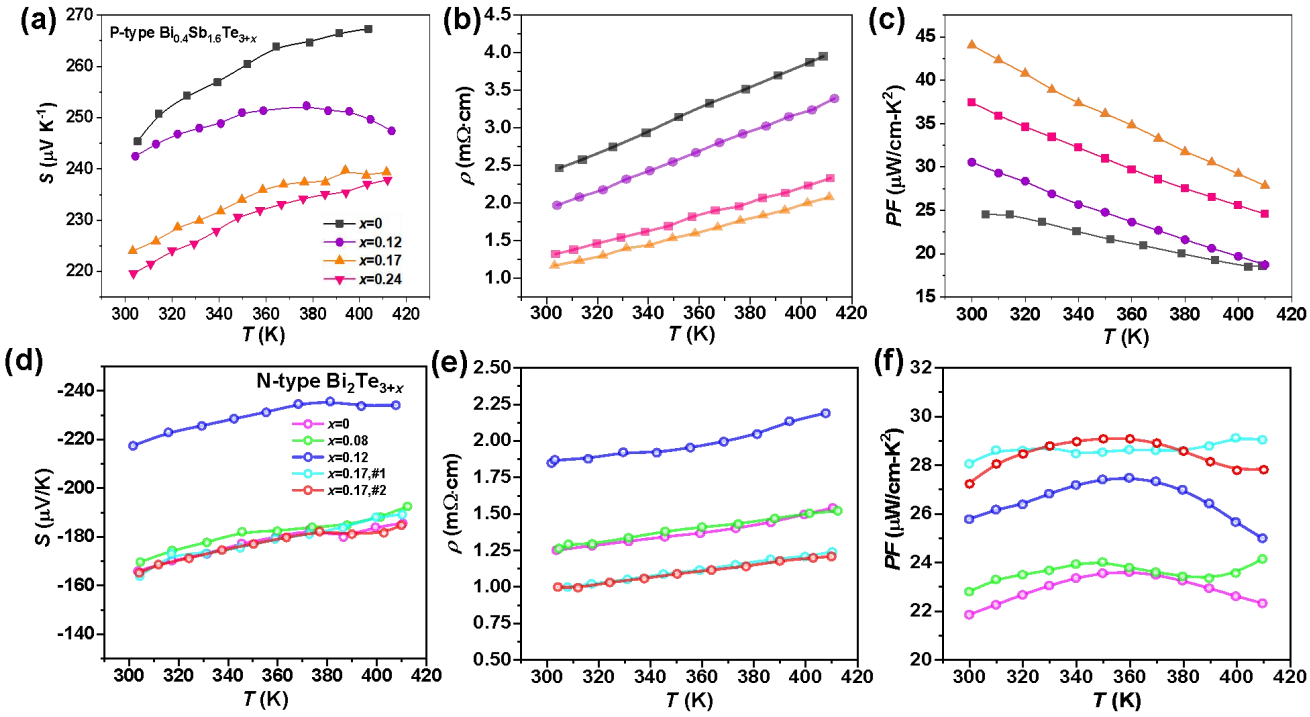

Fig. S13. **Electrical properties for n- and p-type Bi_2Te_3-based films.** The temperature dependent Seebeck coefficient, resistivity and power factor for *p*-type $Bi_{0.4}Sb_{1.6}Te_{3+x}$ (x=0, 0.12, 0.17 and 0.24) (a~b) and *n*-type Bi_2Te_{3+x} (x=0, 0.08,0.12 and 0.17) (c~d) films in this work. The data of parallel samples #1 and #2 show good consistency in electrical properties

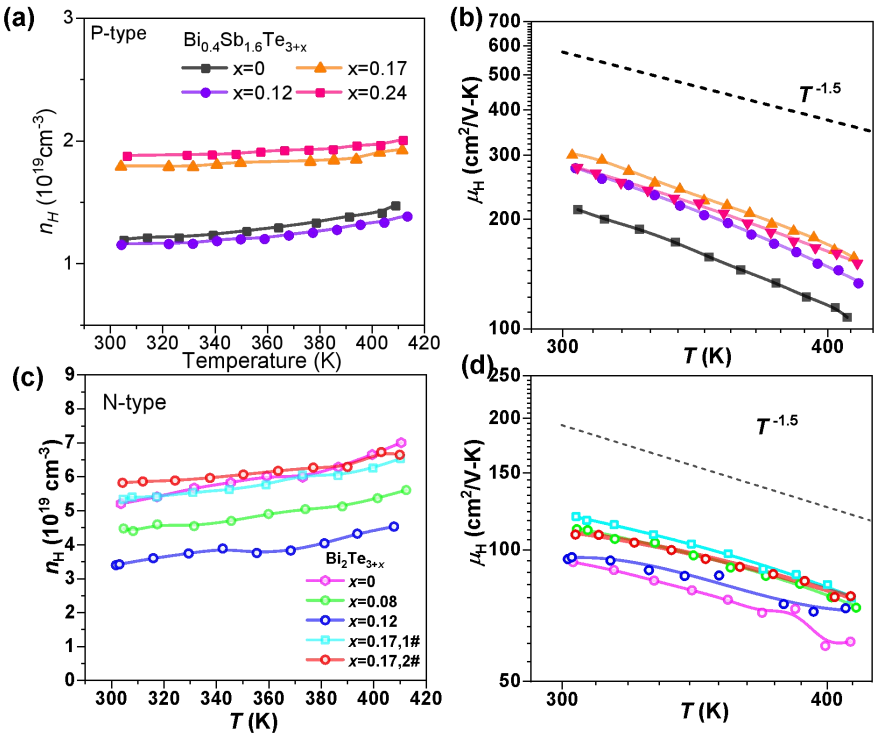

Fig. S14. **Electrical properties for p- and n-type Bi_2Te_3-based samples.** The temperature dependent hall carrier concentration and hall mobility for *p*-type $Bi_{0.4}Sb_{1.6}Te_{3+x}$ (x=0, 0.12, 0.17 and 0.24) (a~b) and *n*-type Bi_2Te_{3+x} (x=0, 0.08, 0.12 and 0.17) (c~d) films in this work. The $T^{-1.5}$ temperature dependence of hall mobility indicated the dominated acoustic phonon scattering in this work.

Supplementary

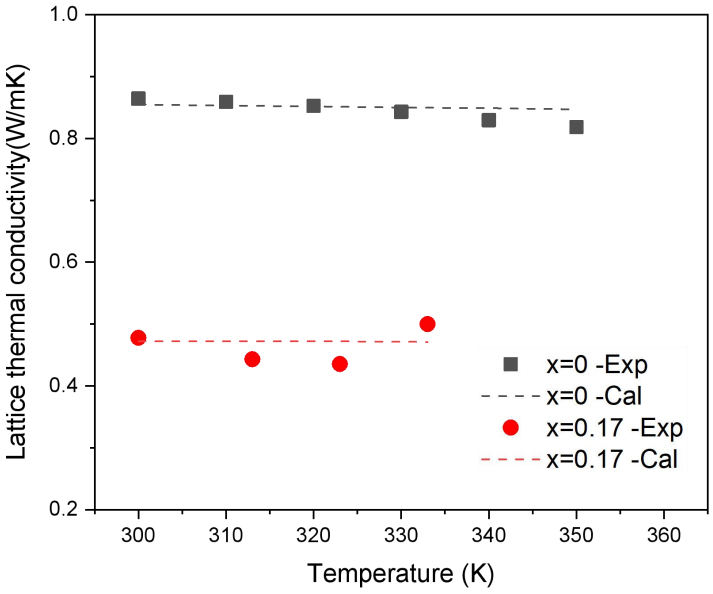

Fig. S15. **The calculated Lattice thermal conductivity properties for *p*-type $Bi_{0.4}Sb_{1.6}Te_{3+x}$ (*x*=0 and 0.17)**. The experimental data are showed by scatter dots and the lines are the calculated results according to Debye-Callaway model.

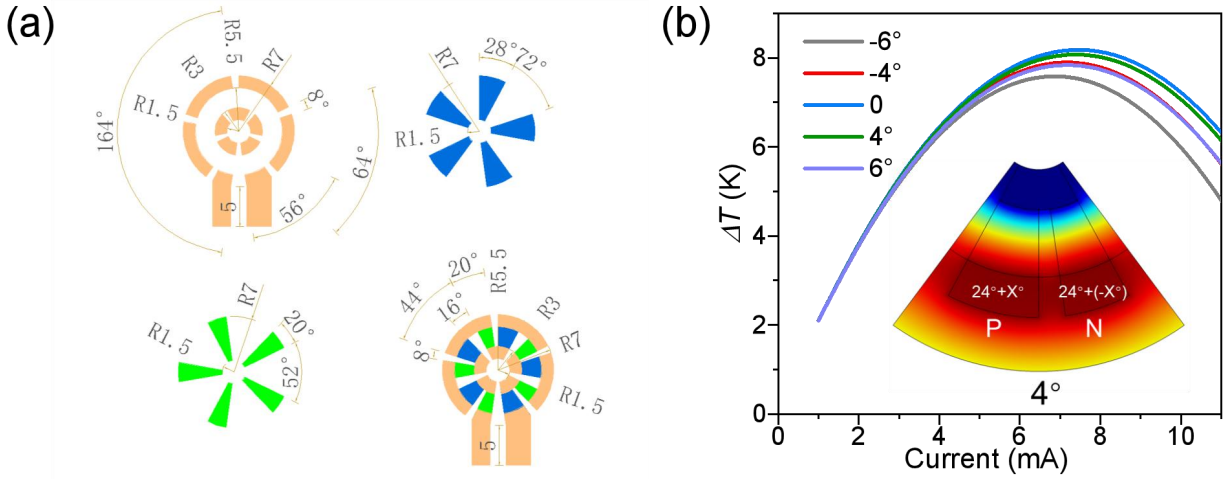

Fig.S16. **Planar device size and simulation process.** The optimized geometry size of the planar device (a), and simulated temperature difference when changing p and n leg angle (b).

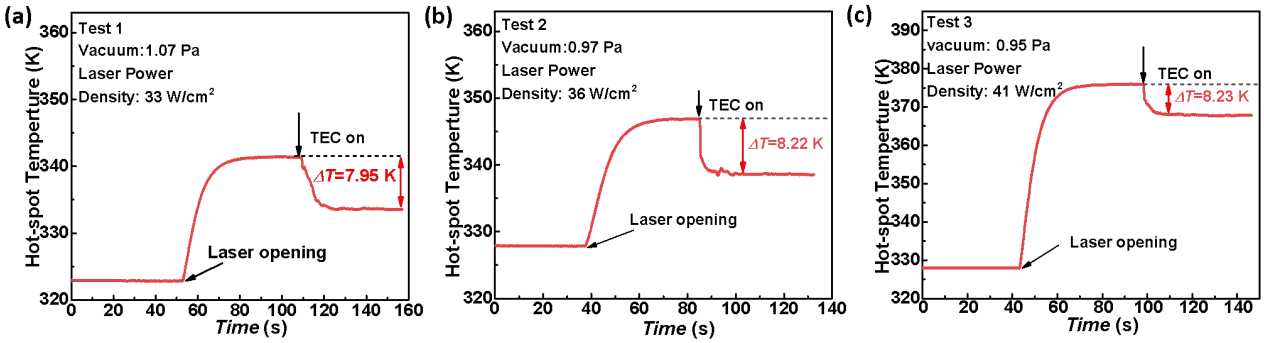

Fig. S17. **Cooling ability of planar f-TEC for laser heating hot spot.** The cooling ability of the f-TEC device prepared in this work measurement with difference laser heating power. Three times test results show ~8 K temperature cooling.

Supplementary

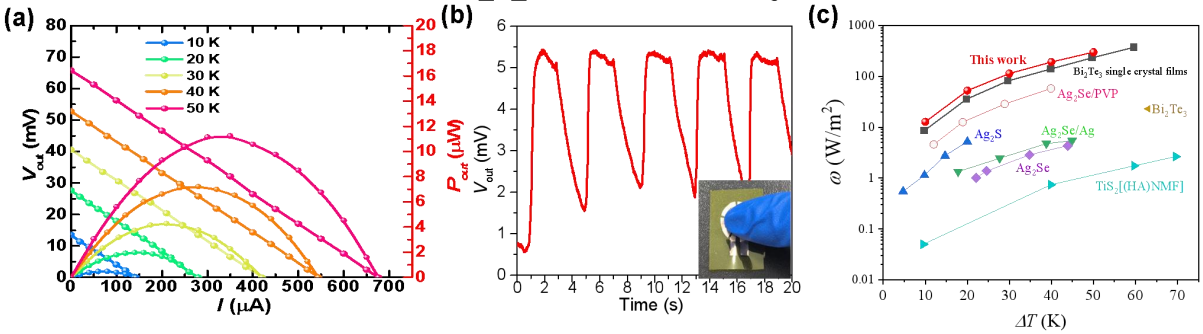

Fig. S18. **Output power of planar film thermoelectric device.** The current dependent voltage and output power at different temperature different (a), and the body heating generated voltage at room temperature (b) of the film thermoelectric device prepared in this work. the output power density of various of film TEGs published (c)[12,17,25-29].

Table S1. The final compositions of p-type $Bi_{0.4}Sb_{1.6}Te_{3+x}$ and n-type Bi_2Te_{3+x} films determined by EDS.

Samples	Extra Te content	Bi(at%)	Sb(at%)	Te(at%)
$Bi_{0.4}Sb_{1.6}Te_{3+x}$	x=0	8.81	33.92	57.26
	x=0.12	8.67	32.18	59.14
	x=0.17	8.17	32.2	59.63
	x=0.24	8.32	32.19	59.48
Bi_2Te_{3+x}	x=0	40.2	-	59.8
	x=0.08	40.3	-	59.7
	x=0.12	40.3	-	59.7
	x=0.17	40.4	-	59.6

Table. S2. The length L, α_{mea}, α_{sub}, α_{con}, α_{TE}, and the final calculated κ_{TE} in thermal diffusion coefficient determination for sample Bi_2Te_{3+x} (x=0 and 0.17).

Sample	***T* (K)**	***L*(mm)**	α_{mea}**(mm²/s)**	α_{sub}**(mm²/s)**	α_{con}**(mm²/s)**	α_{TE}**(mm²/s)**	α_{TE}**(W/mK)**
x=0	300	1.638	1.70	0.33	0.41	0.81	0.98
		1.859	2.08				
		1.953	2.26				
	330	1.638	1.71	0.36	0.43	0.82	0.98
		1.859	2.11				
		1.953	2.25				
	350	1.638	1.74	0.38	0.46	0.87	1.04
		1.859	2.15				
		1.953	2.27				
x=0.17	300	1.766	1.73	0.33	0.45	0.67	0.81
		1.916	1.94				
		1.529	1.43				
		1.702	1.68				
		1.785	1.79				
	330	1.529	1.47	0.36	0.49	0.73	0.88
		1.702	1.71				

		1.785	1.82				
		1.637	1.74				
	350	1.859	2.15	0.38	0.51	0.75	0.90
		1.953	2.27				

Table. S3. **The L, α_{mea}, α_{sub}, α_{con}, α_{TE}, and the final calculated κ_{TE} in thermal diffusion coefficient determination for sample $Bi_{0.4}Sb_{1.6}Te_{3+x}$ (x=0, 0.12, 0.17 and 0.24).**

Sample	T (K)	L(mm)	α_{mea}(mm²/s)	α_{sub}(mm²/s)	α_{con}(mm²/s)	α_{TE}(mm²/s)	α_{TE}(W/mK)
		0.938	0.60				
	300	1.283	0.60	0.32	0.49	0.77	1.06
		2.313	0.99				
		0.938	0.58				
	325	1.283	0.76	0.35	0.50	0.75	1.04
x=0		2.313	1.19				
		0.938	0.60				
	350	1.283	0.75	0.37	0.50	0.72	0.99
		2.313	1.22				
		0.938	0.60				
		0.454	0.46				
x=0.12	300	1.018	1.20	0.32	0.48	0.74	1.02
		1.814	2.31				
		2.559	4.09				
		0.494	0.51				
	300	0.812	0.65	0.32	0.46	0.68	0.89
		1.575	1.06				
		2.592	2.16				
		0.494	0.50				
	313	0.812	0.64	0.35	0.46	0.65	0.85
		1.575	1.10				
		2.592	2.15				
		0.494	0.52				
	323	0.812	0.63	0.35	0.46	0.63	0.83
		1.575	1.13				
x=0.17		2.592	2.23				
		0.494	0.55				
	333	0.812	0.64	0.36	0.49	0.69	0.91
		1.575	1.22				
		2.592	2.32				
		0.494	0.58				
	343	0.812	0.66	0.37	0.50	0.71	0.93
		1.575	1.21				
		2.592	2.40				
		0.494	0.62				
	353	0.812	0.67	0.38	0.52	0.76	0.99
		1.575	1.33				
		2.592	2.56				
		1.575	0.72				
x=0.24	300	2.592	0.93	0.32	0.51	0.80	1.06

Supplementary

	0.494	1.42				
	0.812	0.78				
325	1.575	0.96	0.35	0.51	0.76	1.02
	2.592	1.57				
	0.738	0.76				
350	1.126	1.40	0.38	0.58	0.92	1.24
	1.591	2.24				

Table S4. The Fitting Results according to Debye-Callaway Model for *p*-type $Bi_{0.4}Sb_{1.6}Te_{3+x}$(*x*=0 and0.17).

Samples	L(μm)	$A(10^{-41}\ s^3)$	$B\ (10^{-18}\ sK^{-1})$	$C(10^{-31}\ s^2)$	$D(10^{-3})$	$E(10^{-15}\ s)$
$Bi_{0.4}Sb_{1.6}Te_3$	0.21	2.74	1.70	1.03	1.81	4.50
$Bi_{0.4}Sb_{1.6}Te_{3+0.17}$	5.41	3.91	1.70	4.48	7.88	8.99

Table S5. Parameters Used for the Debye-Callaway Model

Parameters	Description	Values
θ_D	Debye temperature	164 K[17]
v_l	Longitudinal sound velocity	2800 m/s[17]
v_t	Transverse sound velocity	1660 m/s[17]
v_s	Average sound speed	1778 m/s[17]
r	Poisson's ratio	0.24[18]
L	Average grain size	5.41 μm for *x*=0.17 sample
		0.21 μm for *x*=0 sample
$\bar{v}$	Average atomic volume	3.48×10^{-29} m^3
$\bar{M}$	Average atomic mass	2.66×10^{-25} kg
γ	Gruneisen parameter	1.5[19]
Γ	Point defect scattering parameter	0.053
B	Van der waals gap	2.52 Å
N_d	Dislocation density	5.56×10^{16} m^{-2} for *x*=0.17 sample (fitted)
		1.28×10^{16} m^{-2} for *x*=0 sample(fitted)
N_s	Number of staggered layers in a line of unit length	1.66×10^{8} m^{-1} for *x*=0.17 sample(fitted)
		0.80×10^{8} m^{-1} for *x*=0 sample(fitted)

Supplementary references:

1. Zhou Z, Uher C. Apparatus for Seebeck coefficient and electrical resistivity measurements of bulk thermoelectric materials at high temperature. *Rev Sci Instrum* 2005, **76**(2)**:** 023901.
2. Wang T, Wang X, Guo J, Luo Z, Cen K. Characterization of thermal diffusivity of micro/nanoscale wires by transient photo-electro-thermal technique. *Applied Physics A* 2007, **87**(4)**:** 599-605.
3. G. Kresse, J. Furthmüller, Efficiency of ab-initio total energy calculations for metals and semiconductors using a plane-wave basis set, Comput. Mater. Sci. 6 (1996) 15-50. https://doi.org/10.1016/0927-0256(96)00008-0.
4. G. Kresse, J. Hafner, Ab initio molecular dynamics for liquid metals, Phys. Rev. B 47 (1993) 558-561. https://doi.org/10.1103/PhysRevB.47.558.
5. G. Kresse, J. Hafner, Ab initio molecular-dynamics simulation of the liquid-metal--amorphous-semiconductor transition in germanium, Phys. Rev. B 49 (1994) 14251-14269. https://doi.org/10.1103/PhysRevB.49.14251.
6. J.P. Perdew, K. Burke, M. Ernzerhof, Generalized Gradient Approximation Made Simple, Phys. Rev. Lett. 77

Supplementary

(1996) 3865-3868. https://doi.org/10.1103/PhysRevLett.77.3865.
7. M.J. Yao, Y.X. Wang, X. Li, Y. Sheng, H.Y. Huo, L.L. Xi, J. Yang, W.Q. Zhang, Materials informatics platform with three dimensional structures, workflow and thermoelectric applications, Sci. Data 8 (2021) 236. https://doi.org/10.1038/s41597-021-01022-6.
8. P.V.C. Medeiros, S. Stafström, J. Björk, Effects of extrinsic and intrinsic perturbations on the electronic structure of graphene: Retaining an effective primitive cell band structure by band unfolding, Phys. Rev. B 89 (2014) 041407. https://doi.org/10.1103/PhysRevB.89.041407.
9. P.V.C. Medeiros, S.S. Tsirkin, S. Stafström, J. Björk, Unfolding spinor wave functions and expectation values of general operators: Introducing the unfolding-density operator, Phys. Rev. B 91 (2015) 041116. https://doi.org/10.1103/PhysRevB.91.041116.
10. C. Persson, Y.J. Zhao, S. Lany, A. Zunger, n-type doping of CuInSe2 and CuGaSe2, Phys. Rev. B 72 (2005) 035211. https://doi.org/10.1103/PhysRevB.72.035211.
11. S.B. Zhang, The microscopic origin of the doping limits in semiconductors and wide-gap materials and recent developments in overcoming these limits: a review, J. Phys.: Condens. Matter 14 (2002) R881-R903. https://doi.org/10.1088/0953-8984/14/34/201.7. Lu Y, Zhou Y, Wang W, Hu M, Huang X, Mao D*, et al.* Staggered-layer-boosted flexible Bi(2)Te(3) films with high thermoelectric performance. *Nat Nanotechnol* 2023.
12. Lu Y, Zhou Y, Wang W, Hu M, Huang X, Mao D*, et al.* Staggered-layer-boosted flexible Bi(2)Te(3) films with high thermoelectric performance. *Nat Nanotechnol* 2023.
13. Tan M, Deng Y, Hao Y. Enhanced thermoelectric properties and layered structure of Sb2Te3 films induced by special (0 0l) crystal plane. *Chem Phys Lett* 2013, **584:** 159-164.
14. Varghese T, Dun C, Kempf N, Saeidi‐Javash M, Karthik C, Richardson J*, et al.* Flexible Thermoelectric Devices of Ultrahigh Power Factor by Scalable Printing and Interface Engineering. *Adv Funct Mater* 2019, **30**(5).
15. Wang L, Zhang Z, Liu Y, Wang B, Fang L, Qiu J*, et al.* Exceptional thermoelectric properties of flexible organic-inorganic hybrids with monodispersed and periodic nanophase. *Nat Commun* 2018, **9**(1)**:** 3817.
16. An CJ, Kang YH, Song H, Jeong Y, Cho SY. High-performance flexible thermoelectric generator by control of electronic structure of directly spun carbon nanotube webs with various molecular dopants. *Journal of Materials Chemistry A* 2017, **5**(30)**:** 15631-15639.
17. Zheng Z-H, Shi X-L, Ao D-W, Liu W-D, Li M, Kou L-Z*, et al.* Harvesting waste heat with flexible Bi2Te3 thermoelectric thin film. *Nature Sustainability* 2022, **6**(2)**:** 180-191.
18. Jin Q, Jiang S, Zhao Y, Wang D, Qiu J, Tang DM*, et al.* Flexible layer-structured Bi(2)Te(3) thermoelectric on a carbon nanotube scaffold. *Nat Mater* 2019, **18**(1)**:** 62-68.
19. Lu Y, Qiu Y, Cai K, Li X, Gao M, Jiang C*, et al.* Ultrahigh performance PEDOT/Ag2Se/CuAgSe composite film for wearable thermoelectric power generators. *Materials Today Physics* 2020, **14**.
20. Wan C, Tian R, Kondou M, Yang R, Zong P, Koumoto K. Ultrahigh thermoelectric power factor in flexible hybrid inorganic-organic superlattice. *Nat Commun* 2017, **8**(1)**:** 1024.
21. Shang HJ, Ding FZ, Deng Y, Zhang H, Dong ZB, Xu WJ*, et al.* Highly (00l)-oriented Bi(2)Te(3)/Te heterostructure thin films with enhanced power factor. *Nanoscale* 2018, **10**(43)**:** 20189-20195.
22. Hong M, Chasapis TC, Chen ZG, Yang L, Kanatzidis MG , Snyder GJ, Zou J , n-Type $Bi_2Te_{3-x}Se_x$ Nanoplates with Enhanced Thermoelectric Efficiency Driven by WideFrequency Phonon Scatterings and Synergistic Carrier Scatterings, *ACS Nano*, 2016, **10**(4):4719-4727.
23. Bao X, Hou SH, Wu ZX , Wang XD, Yin L, Liu YJ, He HL, Duan SC, Wang BL, Mao J, Cao F, Zhang Q, Mechanical properties of thermoelectric generators, *Journal of Materials Science & Technology* 2023,**148**:64‐74.
24. Wang Y, Liu WD, Gao H,Wang LJ, Li M, Shi XL ,Hong M,Wang H, Zou J, Chen ZG, High Porosity in Nanostructured n-Type Bi_2Te_3 Obtaining Ultralow Lattice Thermal Conductivity, *ACS Applied Materials & Interfaces*,2019, **11**(34):31237-31244.
25. Lu Y. et al. Ultrahigh power factor and flexible silver selenide-based composite film for thermoelectric devices. *Energy Environ. Sci.* 2020, **13**, 1240–1249
26. Ding Y. et al. High performance n-type Ag_2Se film on nylon membrane for flexible thermoelectric.power generator. *Nat. Commun.* 2019, **10**, 841
27. Liang J. et al. Flexible thermoelectrics: from silver chalcogenides to full-inorganic devices. *Energy Environ. Sci.* 2019, **12**, 2983–2990
*2*8. Jiang C. et al. Ultrahigh performance polyvinylpyrrolidone/Ag2Se composite thermoelectric film for flexible energy harvesting. *Nano Energy* 2021, **80**, 105488
29.Tian R. et al. A solution-processed TiS2/organic hybrid superlattice film towards flexible thermoelectric devices. *J. Mater. Chem. A* 2017, **5**, 564–570